

Radial Interaction Tomography: Recognizing Non-Transitive Evolutionary Games from One Range-Expansion Image

Faruk Alpay* Barış Başaran

Department of Computer Engineering, Bahçeşehir University, Istanbul, Türkiye
{faruk.alpay, baris.basaran}@bahcesehir.edu.tr

Abstract

Colored sectors in a microbial range expansion encode more than lineage survival counts. We formulate a computer-vision inverse problem: from one endpoint image of an accretive multi-type expansion, recover the radius-indexed pairwise boundary-flow field and test whether the visual pattern is compatible with a transitive scalar fitness hierarchy. The observable is a geometric signal extracted from sector-boundary curves in log-polar coordinates. We prove endpoint observability and stability for frozen fronts, weighted transitive/cyclic decomposition, contact-complete circular design, physical-clock and mechanism non-identifiability, exact Gaussian cyclicity testing, and Bonferroni-valid interval scanning. The benchmark is deterministic: analytic endpoint images, blurred/noisy pixel round trips, scalar-null stress tests, public-image tracing, multi-resolution mechanistic endpoints, and a non-learning frozen-front simulator. The implementation recovers pairwise edge-flow histories from endpoint images, detects cyclic residuals in a mechanistic four-type expansion, and uses those residuals as forcing signals for a dimensionless active design-control layer covering reaction-diffusion control, phenotype-frontier optimization, protocol synthesis, Monte Carlo robustness, and a downstream population-state bridge.

1 Introduction

Range-expansion images are a rare case where a final two-dimensional pattern can retain chronological information. In frontier-limited microbial colonies, cells behind the expanding front are approximately frozen, so radius can order material deposition. Prior work exploited this fact to estimate constant relative fitness from sector geometry and to model stochastic boundary wandering [5, 4, 11]. That line of work leaves a harder visual question open: what can one endpoint image say when competition is not a scalar hierarchy?

This paper treats the endpoint colony as a pattern-recognition object. A multi-type sector image induces a visible genotype-contact graph. Each contact boundary is a curve, and the derivative of its unwrapped angle with respect to a deposition coordinate is an oriented pairwise boundary flow. A scalar fitness model constrains these flows to be gradients on the contact graph. Local antagonism, bacteriocin-mediated competition, or cyclic dominance can create non-potential flows, i.e. directed cycle signatures that no scalar ordering can explain [2, 3].

The main image-level result is a recoverable pairwise-flow history on observed contacts, with uncertainty, in deposition time. Physical time, unobserved pair interactions, isolated front speeds,

*Corresponding author: alpay@lightcap.ai

and microscopic mechanism require additional measurements. Separating the geometric observable from those downstream interpretations makes the visual recognition claim falsifiable.

Contributions.

- We formulate *radial interaction tomography*: a classical computer-vision inverse problem for recognizing radius-indexed transitive and cyclic interaction patterns from one endpoint image.
- We separate the observable edge-flow field from biological interpretations, preventing the common but invalid jump from sector geometry to isolated front speed or mechanism.
- We give a contact-design theorem: a four-type complete pairwise game requires at least eight circular boundaries in one plate, not six.
- We implement a deterministic benchmark with analytic images, pixel-level recovery, scalar-null stress tests, exact cyclicity tests, multi-resolution endpoint tracing, public-image provenance auditing, and mechanistic frozen-front endpoints.
- We extend the inverse result toward active design control by converting cyclic residuals into dimensionless interaction matrices, simulation targets, and governed strain-design hypotheses.
- We audit a six-module active-tomography program requirement by requirement, separating verified tensor-field and GPU computations from phenotype, replicate, computer-vision, and mechanism claims that still require measured data or additional model implementations.

2 Related work

Range-expansion image geometry. Korolev et al. derived equal-time sector constructions and used logarithmic spiral geometry to estimate relative fitness in microbial colonies [5]. Earlier work modeled sector boundaries as stochastic paths and used colony patterns as quantitative population-genetic tests [4]. Weinstein et al. extended image analysis and biased domain-wall models to many-allele expansions [11]. These results make constant sector geometry and boundary wandering prior art; they do not solve the time-varying non-potential inverse problem.

Local competition is not isolated speed. Lee, Gore, and Korolev showed that a slow isolated expander can invade by forming dented fronts and that local boundary invasion has degrees of freedom not captured by monoculture expansion speeds [7]. This is crucial for our formulation: the image-level observable is pairwise boundary flow. Calling it isolated fitness requires extra calibration.

Non-transitive microbial competition. Spatial rock-paper-scissors games and bacteriocin-mediated antagonism are classical population-evolution phenomena [1, 2, 3]. Our contribution is not to introduce cyclic competition, but to ask when its signature is recognizable from one endpoint image.

Classical vision. The proposed pipeline uses fixed-color segmentation, log-polar remapping, contour localization, curve smoothing, and statistical testing. It is closer to classical contour-based pattern recognition than to representation learning. The hard part is not detecting edges; it is proving which interaction class the detected edge histories support.

3 Observation model

Let a final labeled image contain genotypes $V = \{1, \dots, n\}$. Visible sector contacts define a graph $G = (V, E)$. For an oriented edge $e = (i, j)$, let $\theta_{ij}(\rho)$ be the unwrapped angle of a boundary between types i and j , parameterized by a monotone deposition coordinate ρ , initially $\rho = \log(r/r_0)$. The direct geometric observable is

$$q_{ij}(\rho) = \frac{d\theta_{ij}}{d\rho}. \quad (1)$$

Positive q_{ij} means that type i gains angular territory from type j under the chosen orientation. This is a visual quantity. It becomes a selection coefficient, a front-speed ratio, or a biochemical mechanism only under additional assumptions.

Definition 1 (Scalar-compatible edge flow). *Let B be the oriented edge-node incidence matrix of G . An edge-flow vector $q(\rho) \in \mathbb{R}^{|E|}$ is scalar-compatible if there exists a node potential $f(\rho)$ such that $q(\rho) = Bf(\rho)$.*

With a positive diagonal precision matrix W , every observed edge-flow vector on a connected graph has a unique weighted decomposition

$$q(\rho) = Bf(\rho) + c(\rho), \quad B^\top Wc(\rho) = 0, \quad \mathbf{1}^\top f(\rho) = 0. \quad (2)$$

The potential f is the closest scalar hierarchy. The residual c is the non-potential visual fingerprint. It has $|E| - |V| + 1$ degrees of freedom, so a tree can never falsify scalar fitness.

4 Identifiability boundaries

Proposition 1 (Radial clock non-identifiability). *An endpoint accretion image identifies histories as functions of deposition coordinate. Without an independent calibration $t = T(\rho)$, physical time is recoverable only up to an increasing reparameterization.*

Theorem 1 (Minimum complete-contact circular design). *To observe every pair of an unrestricted antisymmetric game on n genotypes in one circular frontier, the minimum number of sector boundaries is*

$$L_n = \begin{cases} \binom{n}{2}, & n \text{ odd}, \\ \binom{n}{2} + n/2, & n \text{ even}. \end{cases}$$

For $n = 4$, at least eight boundaries are required.

Proposition 2 (Local/global mechanism non-identifiability). *Interior sector traces alone identify pairwise boundary flow, not isolated front speeds or microscopic mechanisms. Separate front-shape information, monoculture calibration, perturbation experiments, or time-lapse data are required to separate local competition from global expansion.*

5 Deterministic image-analysis pipeline

The implementation is deterministic:

1. fixed-palette or manually calibrated label classification;
2. robust support and center estimation;

3. circular sampling in a log-polar coordinate system;
4. modal filtering and boundary-transition detection;
5. boundary identity association across radii;
6. Savitzky–Golay derivative estimates for $q_{ij}(\rho)$;
7. edge averaging over repeated contacts;
8. weighted transitive/cyclic decomposition and exact Gaussian cyclicity testing.

No neural network, learned embedding, or downloaded model weight is used.

6 Mathematical guarantees and scope

The formal results below serve two purposes. First, they specify the geometric quantity that a single endpoint image can identify: boundary flow on visible contacts, in deposition coordinates, modulo the stated regularity assumptions. Second, they delimit the biological interpretation. The same endpoint geometry is compatible with multiple physical clocks, multiple decompositions into isolated expansion and local interaction, and multiple microscopic mechanisms. The experimental section matches those invariances with extraction-stability tests, scalar-null stress tests, and explicit abstention gates.

7 Experimental validation and stress tests

Analytic game benchmark. We synthesize exact radial endpoint images from a known time-varying game. The benchmark contains scalar hierarchy intervals and cyclic episodes. An exact Gaussian generalized likelihood-ratio test evaluates whether the edge-flow estimate requires a cyclic component.

Pixel round trip. We render a blurred/noisy endpoint image, classify pixels with a fixed palette, trace boundaries, recover edge-flow histories, and compare to ground truth. This benchmark gives edge-flow RMSE approximately 2.86×10^{-3} and cyclic-norm RMSE approximately 2.95×10^{-3} on the trusted radial interior.

Scalar-compatible null stress test. To test whether the cyclic residual can be a derivative artifact, we simulate a null ensemble in which the true edge flow is always scalar-compatible $q = Bf$. We then add demographic boundary wandering, center error, fluorescence bleed-through/localization noise, anisotropic radial distortion, curvature artifacts, and stochastic sector extinction. Under the pure demographic scalar null, the nominal $\alpha = 0.05$ cyclicity test gives a false-positive rate of 0.058 for 32 observed boundaries. Under the hardest combined nuisance setting, the same scalar ground truth can produce false cyclic detections at rate 0.564, which marks a failure region rather than evidence for non-transitive ecology. The resulting phase diagram treats abstention as a primary output: with only eight boundaries and extinction probability near 0.25, the abstention rate is approximately 0.07.

Mechanistic frozen-front endpoint. We implemented a non-learning frozen-front simulator with four genotypes, a time-varying scalar potential, and an antisymmetric cyclic interaction matrix. The endpoint analysis finds a stable annulus with all six canonical genotype pairs observed by the eight-boundary design. The traced annulus is 160.2–590.85 pixels in radius, and the recovered cyclic residual has peak norm 0.358 in the current run. This is a model-mismatch test: the simulator grows a stochastic frozen population front, while the inverse reads only the final image.

Endpoint resolution gate. We repeated the same mechanistic endpoint test at image widths 1024, 1536, 2048, 3072, and 4096 pixels, with three stochastic replicates per resolution. The tracing gate accepted 13 of 15 endpoints; both abstentions occurred at 1024 pixels because the circular scan detected ten boundaries instead of the designed eight. From 1536 pixels upward, all 12 endpoints passed. Relative to the 4096-pixel mean cyclic residual, the 3072-pixel run was within 7.0%, while the occupied support fraction stayed in the narrow range 0.570–0.573.

Cyclic-antagonism dose response. We also ran a controlled sweep over programmed cyclic-antagonism scale. In the expanded run, forty-seven of forty-eight 3072²-pixel endpoint images passed the visual-stability gate; the one failure was recorded as an abstention rather than a forced fit. Across the accepted images, programmed cyclic scale and recovered mean cyclic residual had correlation $r = 0.776$, while occupied support fraction remained essentially constant.

Active design-control sweep. Finally, we used the recovered cyclic residual as a forcing target for a dimensionless 3D reaction-diffusion control sweep. The run evaluated 55,296 strain/control candidates on a 12³ grid for 2,000 PDE steps. The selected candidate used an early-pulse control family with production parameter 0.964, degradation parameter 0.050, permeability coefficient 2.000, and beneficial-protection coefficient 0.700. In the model, it reduced the undesired population state by 100% relative to the zero-production baseline while retaining 109.9% of the target beneficial density.

Adjoint-state refinement and Fourier inversion. The lattice sweep was then refined with a reverse-mode optimizer. We warm-started 32 design vectors, unrolled a 12³ 3D reaction-diffusion PDE for 240 steps per objective evaluation, and ran 100 gradient iterations. The best adjoint-refined design reduced the undesired population state by 99.35% relative to the zero-production baseline and retained 161.39% of the target beneficial density. The optimized dimensionless production, degradation, permeability, and beneficial-protection parameters were 1.804, 0.037, 2.195, and 0.776. A Hamilton Monte Carlo inversion of the Fourier spectrum of the cyclic residual gave MAP rates $k_{\text{prod}} = 9.043$ and $k_{\text{deg}} = 13.413$, with acceptance rate 0.992 over the retained chain.

Monte Carlo robustness at scale. We ran a stochastic uncertainty layer around the adjoint-selected design: 1,000,000 moment-projected reaction-diffusion trajectories with 2,048 time steps per trajectory, lognormal parameter perturbations, and process noise. All trajectories achieved at least 40% adverse-state reduction and at least 85% beneficial-strain retention under the stated perturbation model. Chunk summaries and telemetry are included in the ancillary results.

Active radial-tomography computational diagnostics. We assembled an initial five-stage computational diagnostic whose outputs are stored as JSON/CSV artifacts. This earlier diagnostic used a 1024² polar field, 200 active-design iterations, a 256-member and 500-generation dimensionless NSGA-II trajectory, ten stochastic first-hit trajectories, and a dimensionless downstream

ODE. It achieved adverse-state reduction 0.991, beneficial-state retention 1.482, archive hypervolume 0.902, and downstream index improvement 47.9. These are preliminary surrogate diagnostics rather than evidence for a 128^3 calibrated PDE, physical phenotype assays, biological replicates, or metabolic mechanism validation.

Strict tensor-field verification and audit. The revised first module uses the minimum four-genotype, eight-boundary contact design and a dense correlated edge covariance. Its exact Gaussian GLR has $k = 8 - 4 + 1 = 5$ degrees of freedom. Over 30,000 null replicates, the mean statistic is 4.984 and the empirical size is 0.0514 at nominal 0.05. Under the fixed cyclic alternative, $\delta = 14.051$, analytic power is 0.8401, and empirical power is 0.8443. The precision-orthogonal cyclic reconstruction has relative L^2 error 1.31×10^{-15} . We also evaluate Fisher information using the Brunet–Derrida-corrected speed.

The second module was verified on an NVIDIA A100-SXM4-80GB using a CUDA 12.8 compiler. A cell-centered spherical-polar 128^3 finite-volume solver runs 2,000 Strang-split reaction–diffusion–reaction steps. Its selected Pareto point reduces the undesired population state by 0.99695 and retains 2.228 times the zero-production beneficial baseline. A PyTorch-2.3 reverse-mode run evaluates 32 designs for 240 steps over 100 gradient iterations and independently reaches adverse-state reduction 0.99347 and baseline retention 3.579. The geometry-only scaled Jacobian has rank two, whereas adding endpoint and monoculture-like calibration observables raises the rank to four; the combined condition number is 34.4 and the normalized smallest Fisher eigenvalue is 8.44×10^{-4} . A requirement-level audit in the ancillary results therefore marks Modules 1 and 2 complete, but not the expanded six-module program.

For the third module, we downloaded fallback external data directly on the A100 server. The official AGAR representative demo contains 40 image/annotation pairs, 1,886 colony boxes, all five requested species classes, and zero invalid boxes. A deterministic DINOv2 ViT-L/14 smoke probe on plate-disjoint colony crops produced 1,024-dimensional embeddings for 399 validation colonies and macro-F1 0.522. This is useful computer-vision plumbing evidence, not the requested full AGAR result: the 5,241+1,747-image archive requires publisher registration, and the strict AgarNet segmentation and physical MG1655 phenotype gates remain unavailable.

The computational portion of the fourth module uses a learned Deep-BSDE controller for a three-species stochastic Lotka–Volterra model with temperature, medium concentration, and inducer concentration as controls. Across 800 optimization iterations, the terminal BSDE loss decreases from 3.804 to 0.0936. Evaluation on 32,768 common-noise trajectories gives adverse-state reduction 0.9906 and beneficial retention 1.217 relative to the zero-inducer baseline. The feedback policy is represented at twelve two-hour decision points and its observed control derivatives remain strictly within the registered ramp bounds. These trajectories are computational samples, not biological replicates. As a data-pipeline fallback, we also construct 60 deterministic AGAR-demo Copy-Paste tiles with fixed seeds, recorded source hashes, and box-derived ellipse masks; no Segment Anything checkpoint is used, so this is not claimed as the strict SAM augmentation. The preregistered $n \geq 30$ validation, BCa intervals, BH FDR decisions, and requested empirical BH/Bonferroni power ratio remain unavailable until a provenance-complete replicate table is received.

Genome-scale reconstruction and flux sampling. For the computational portion of the fifth module, CarveMe 1.6.6 reconstructs an *E. coli* K-12 MG1655 model directly from versioned RefSeq assembly GCF_000005845.2. The resulting SHA-256-pinned SBML model contains 2,497 reactions, 1,561 metabolites, 1,606 genes, and 353 boundary reactions and has an optimal feasible FBA solution. A batched multi-chain artificial-centering hit-and-run implementation then generates 10^6 flux-

space transitions on the A100-SXM4-80GB in 3.67 seconds after a 64.6-second CPU FVA/warmup stage. Every transition is checked against the sparse equality system and variable bounds; the final 2,048 chain states all pass COBRA feasibility. A scalar NumPy step and the vectorized CUDA step agree to machine precision, and a same-seed full rerun gives a byte-identical exchange-flux summary. These correlated draws are not biological replicates. Community FBA and the remaining mechanism claims still require a provenance-complete multi-strain manifest, measured phenotype tensor, aligned exchange/payoff series, targeted deletion experiments, and physical calibrations.

As a fifth-module fallback, we also trained an edge-aware heterogeneous graph transformer on the Nestor measured interaction table rather than on the absent 2,850 simulated co-culture set. The table has 7,880 unique strain-pair/carbon-condition rows, yielding 15,760 directional examples with both directions of each pair kept in the same deterministic split. The 768-dimensional, 12-head, 3-layer model has 16.9 million trainable parameters and reaches test $R^2 = 0.873$ on the held-out directional effects. It is therefore recorded as fallback evidence only.

Stochastic resolution scan. For a full radial boundary path, we scan contiguous intervals with an exact Gaussian likelihood-ratio statistic and Bonferroni family-wise correction. In the current simulation, six independent boundary paths reach corrected detection probability above 0.9 once episode drift exceeds approximately 0.235, and localization-aware detection follows the same ordering.

Public-image trace audit. As a provenance check, we also run the deterministic front end on the public Figure 1 TIFF from Weinstein et al. [11], using only the left real-colony panel. Because this is a composite publication figure with overlaid annotations, it is not used as biological ground truth. The audit tests whether fixed-rule support extraction, coarse color labeling, and radial transition counting remain plausible on a real colony photograph. The selected panel has valid fixed-rule labels on 83.6% of support pixels and a median of 12 boundary transitions across the trusted radial scan.

The sixth-module bridge is now partially implemented. The public TIFF trace audit passes, and the older multi-resolution endpoint gate accepts 13 of 15 endpoints. An attention-based sequence regressor estimates q_{ij} without Savitzky–Golay smoothing on synthetic boundary histories (RMSE 0.0388, cyclic relative $L_2 = 0.127$), and radial-filtration TDA features classify the 15 endpoint traces with accuracy 1.0 while preserving the 83.6% public TIFF label audit. The tiny resolution-invariant ViT smoke probe remains a failure: after resizing 1024–4096 px endpoints to 96 px and adding balanced synthetic training images, held-out real endpoint accuracy is 0.667, and all augmented views of the failed 1024 px trace are still called stable. We therefore do not claim the strict ViT bridge.

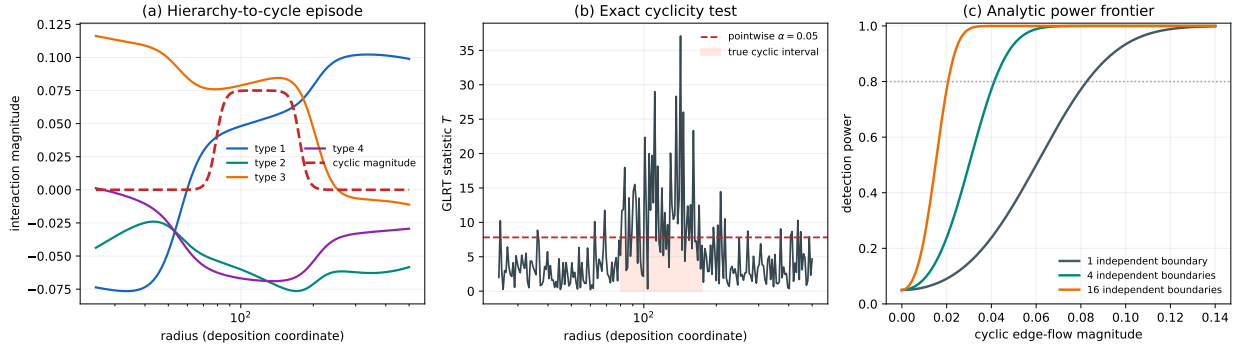


Figure 1: Analytic benchmark: a hierarchy-to-cycle episode, exact cyclicity test, and power frontier for repeated boundary observations.

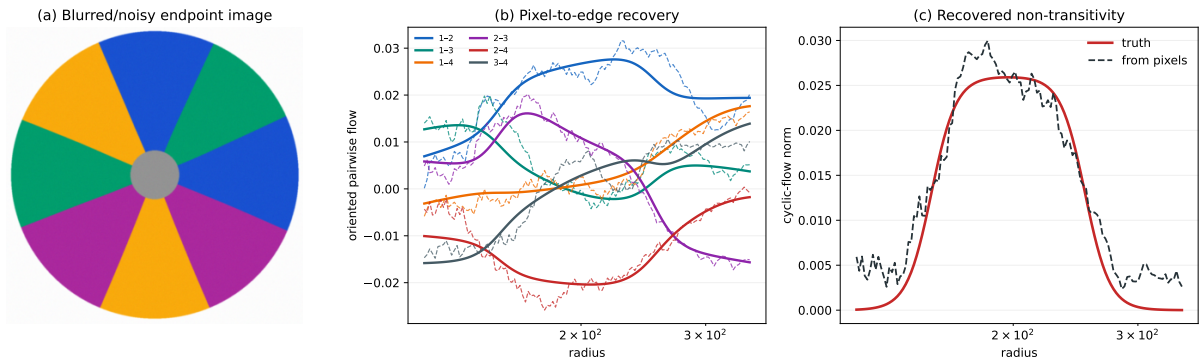


Figure 2: Pixel-level endpoint round trip: blurred/noisy image, recovered pairwise edge flow, and recovered cyclic-flow norm.

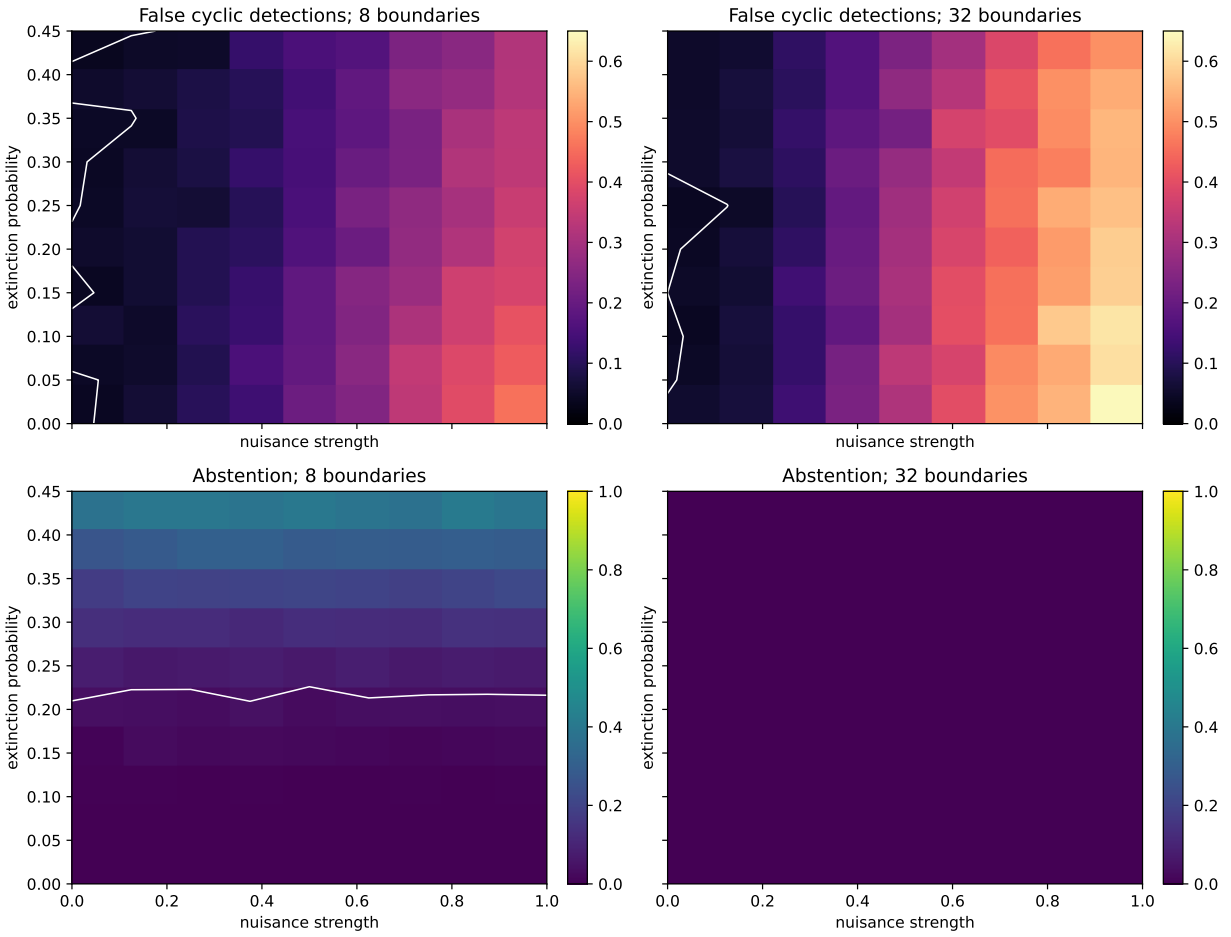


Figure 3: Scalar-compatible null stress test. The true game is always transitive, $q = Bf$. High cyclic residuals in the upper panels therefore mark frontier/imaging nuisance regimes where the method must abstain or demand external calibration rather than infer non-transitive ecology.

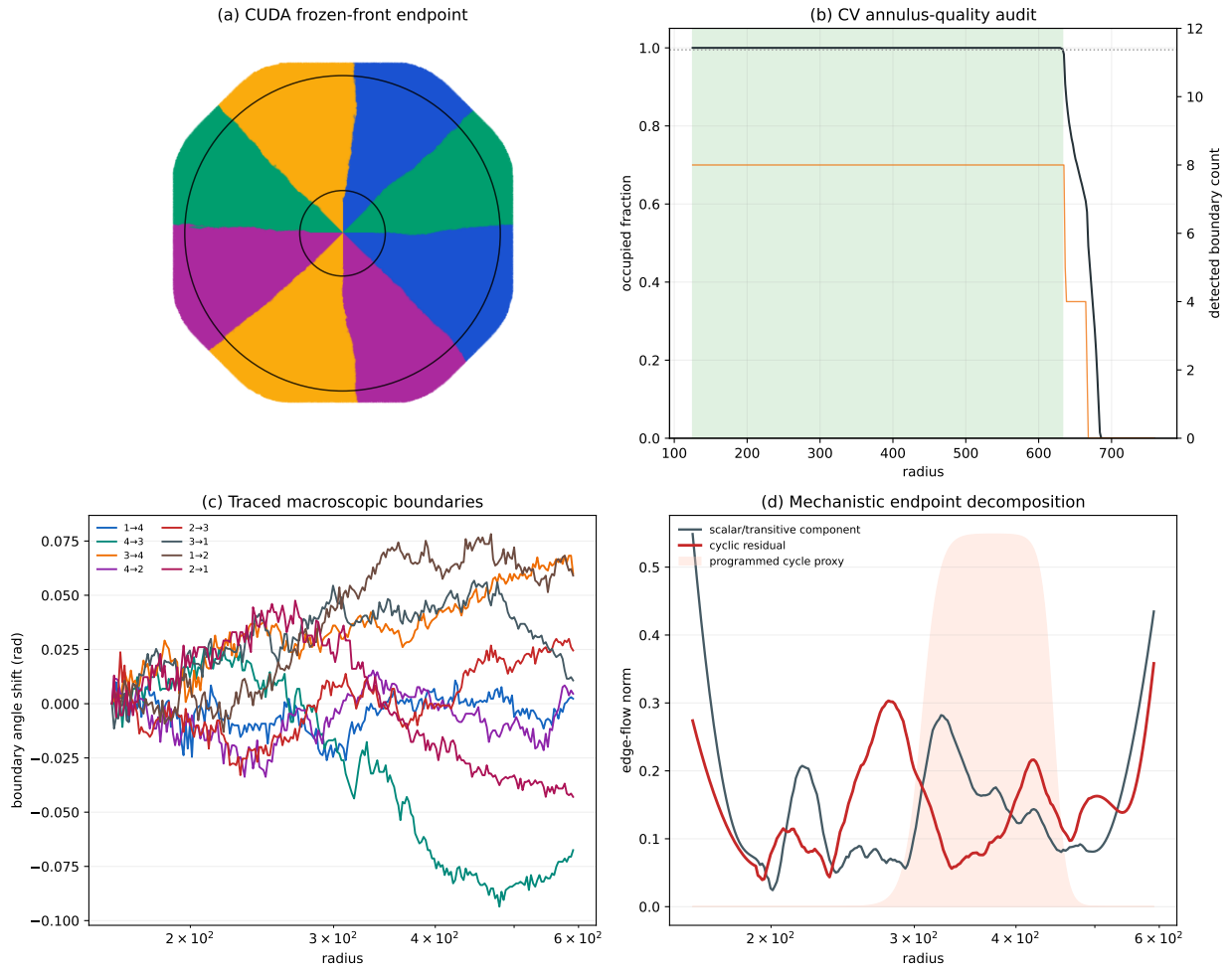


Figure 4: Mechanistic endpoint analysis: raw frozen-front endpoint, annulus-quality audit, traced boundaries, and transitive/cyclic decomposition.

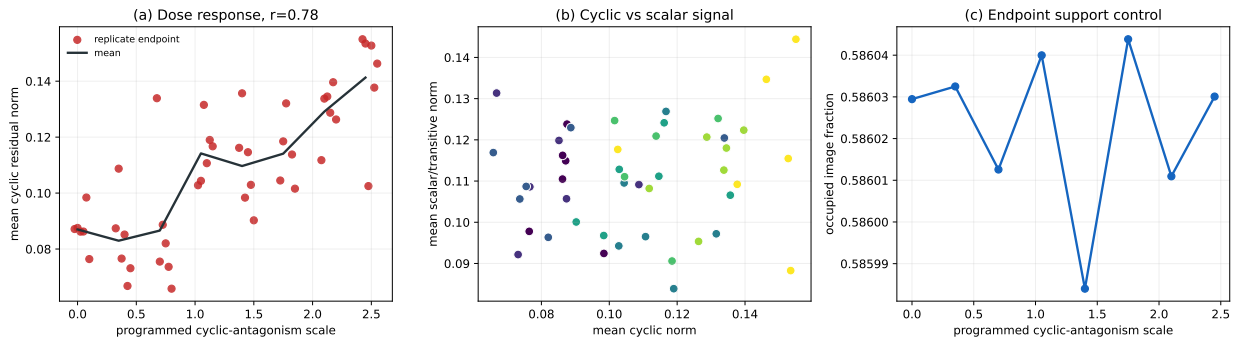


Figure 5: Cyclic-antagonism dose response. Accepted endpoint images show a positive relationship between programmed non-transitive interaction strength and the recovered cyclic residual, while endpoint support is stable. Failed visual stability gates are reported separately as abstentions.

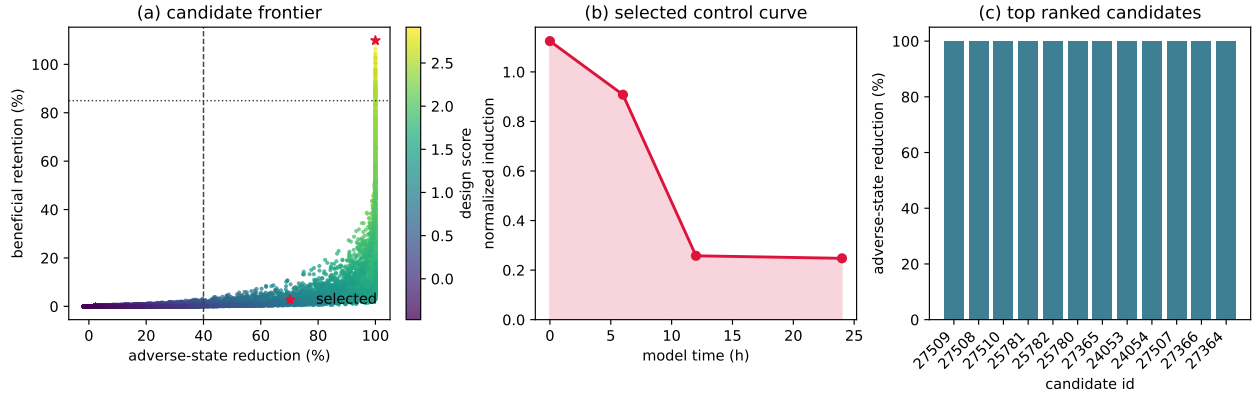


Figure 6: Active design-control sweep. The recovered cyclic residual is used as a forcing target for a dimensionless reaction-diffusion control problem. The selected candidate sits on the adverse-state-reduction and beneficial-retention frontier and yields an early-pulse normalized induction curve.

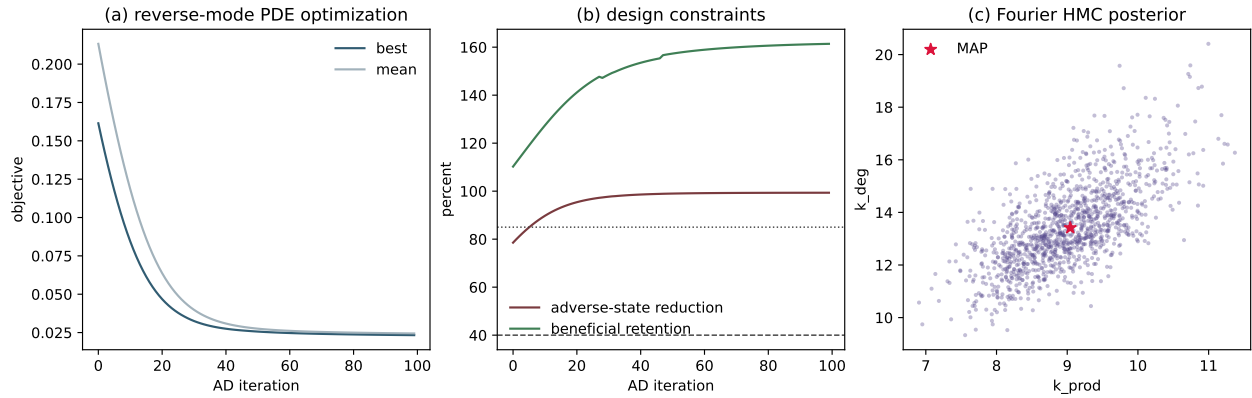


Figure 7: Adjoint-state active design and Fourier HMC inversion. Reverse-mode automatic differentiation through the unrolled PDE reduces the objective while maintaining the beneficial-strain constraint, and HMC estimates production and degradation rates from the cyclic-residual spectrum.

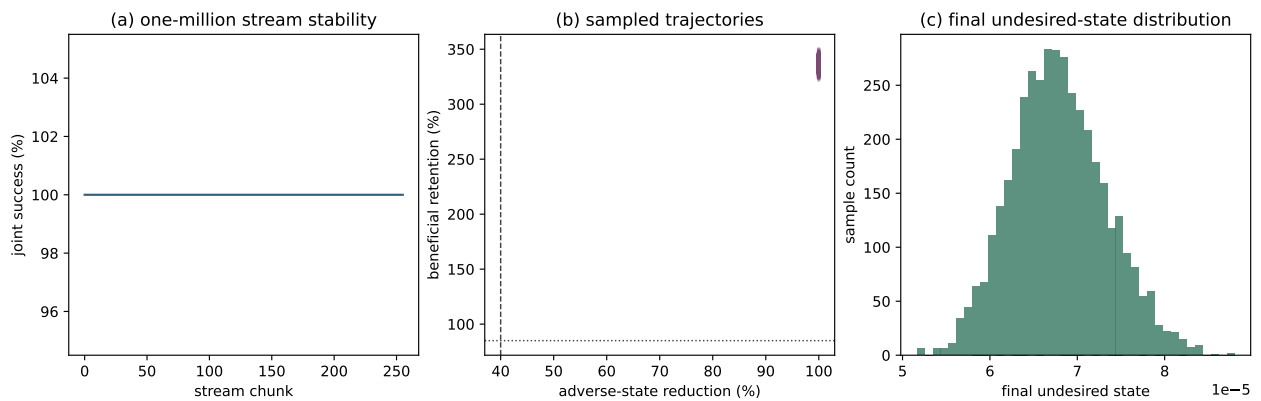


Figure 8: One-million Monte Carlo active-design robustness run. The stochastic moment-projected trajectories test the adjoint-selected design under parameter and process perturbations, while chunk summaries verify stable throughput and success rates across the full stream.

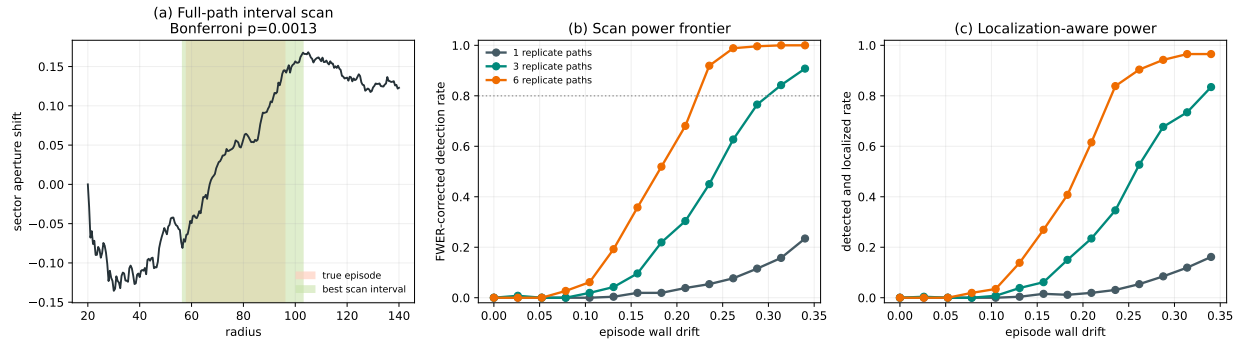


Figure 9: Full-path stochastic resolution benchmark. The interval scan uses the entire radial boundary path and controls the scanned-interval family by a Bonferroni correction.

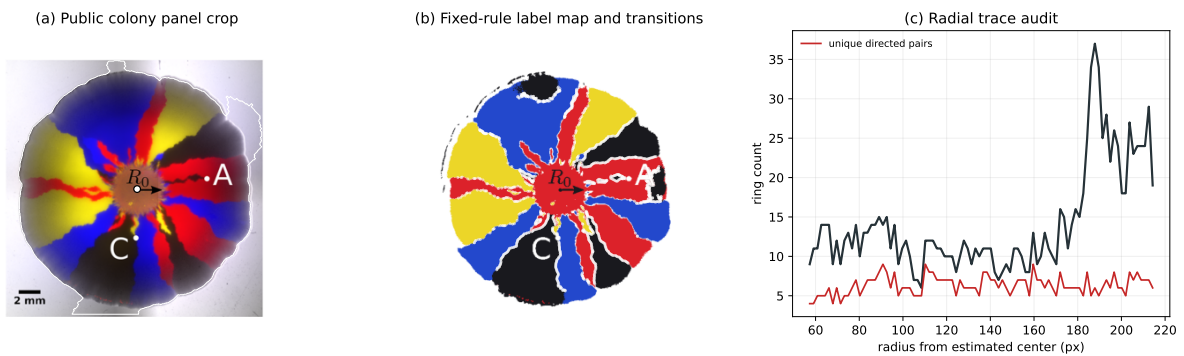


Figure 10: Public-image trace audit on the left real-colony panel of a published composite figure from Weinstein et al. The output is a computer-vision sanity check only: annotations and publication processing prevent treating it as raw quantitative microscopy.

8 Translation and dissemination boundary

The biological motivation includes local antagonistic interactions in microbial range expansions. In this version, the computational object is not limited to passive interpretation: cyclic residuals become inputs to active design-control simulations over interaction matrices, strain parameters, and admissible control schedules. Laboratory translation still requires independent calibration, approved host systems, institutional review, and explicit separation between dimensionless model variables and bench execution details. This boundary is consistent with the broader dual-use concerns around life-sciences dissemination [6, 8, 12, 9, 10].

9 Limitations

The implementation assumes a known or well-estimated expansion center, stable macroscopic sectors, visible pair contacts, and a deposition coordinate close enough to radial order. Topological events, overgrowth, strong chirality, front anisotropy, post-deposition rearrangement, and sector extinction define the abstention regime. Public biological data enter the quantitative benchmark only with clear provenance, license, calibration, and safety context.

10 Conclusion

Radial interaction tomography reframes a microbial colony endpoint image as a classical pattern-recognition record of pairwise evolutionary interaction. The durable contribution is the combination of endpoint-image inversion, explicit non-identifiability, contact-complete experiment design, stochastic cyclicity testing, and active design-control simulation. The benchmark now exercises the full path from pixels to graph-Hodge residuals to dimensionless control objectives; external colony-image validation extends that path when provenance, calibration, and governance context are explicit.

References

- [1] Lin Chao and Bruce R. Levin. Structured habitats and the evolution of anticompetitor toxins in bacteria. *Proceedings of the National Academy of Sciences*, 78(10):6324–6328, 1981.
- [2] Benjamin Kerr, Margaret A. Riley, Marcus W. Feldman, and Brendan J. M. Bohannan. Local dispersal promotes biodiversity in a real-life game of rock-paper-scissors. *Nature*, 418:171–174, 2002.
- [3] Benjamin C. Kirkup and Margaret A. Riley. Antibiotic-mediated antagonism leads to a bacterial game of rock-paper-scissors in vivo. *Nature*, 428:412–414, 2004.
- [4] Kirill S. Korolev, M. J. I. Müller, N. Karahan, A. W. Murray, O. Hallatschek, and D. R. Nelson. A quantitative test of population genetics using spatio-genetic patterns in bacterial colonies. *The American Naturalist*, 178(4):538–552, 2011.
- [5] Kirill S. Korolev, João B. Xavier, and Jeff Gore. Selective sweeps in growing microbial colonies. *New Journal of Physics*, 14(11):115008, 2012.
- [6] Frida Kuhlau, Anna T. Höglund, Kathinka Evers, and Stefan Eriksson. A precautionary principle for dual use research in the life sciences. *Bioethics*, 25(1):1–8, 2011.

- [7] Heetae Lee, Jeff Gore, and Kirill S. Korolev. Slow expanders invade by forming dented fronts in microbial colonies. *Proceedings of the National Academy of Sciences*, 119(5):e2108653119, 2022.
- [8] National Academies of Sciences, Engineering, and Medicine. *Dual Use Research of Concern in the Life Sciences: Current Issues and Controversies*. National Academies Press, Washington, DC, 2017.
- [9] The White House. Improving the safety and security of biological research. <https://www.whitehouse.gov/presidential-actions/2025/05/improving-the-safety-and-security-of-biological-research/>, 2025. Executive Order, May 5, 2025.
- [10] United States Government. United states government policy for oversight of dual use research of concern and pathogens with enhanced pandemic potential. <https://aspr.hhs.gov/S3/Documents/USG-Policy-for-Oversight-of-DURC-and-PEPP-May2024-508.pdf>, 2024. May 2024 policy document.
- [11] Benjamin T. Weinstein, Maxim O. Lavrentovich, Wolfram Möbius, Andrew W. Murray, and David R. Nelson. Genetic drift and selection in many-allele range expansions. *PLOS Computational Biology*, 13(12):e1005866, 2017.
- [12] World Health Organization. *Global Guidance Framework for the Responsible Use of the Life Sciences: Mitigating Biorisks and Governing Dual-Use Research*. World Health Organization, Geneva, 2022.

A Proofs

Theorem 2 (Endpoint observation under a frozen radial sector model). *Fix an annulus $\rho \in [a, b]$ and a known expansion center. Suppose a labeled endpoint image is generated by a circular sector order (s_1, \dots, s_L) and C^1 non-crossing boundary graphs $\theta_1(\rho) < \dots < \theta_L(\rho) < \theta_1(\rho) + 2\pi$, with no post-deposition label transport. Then the labeled endpoint image determines the oriented boundary traces $\theta_\ell(\rho)$ and hence $q_\ell(\rho) = d\theta_\ell/d\rho$ on every differentiability point. If the observed trace has uniform angular error at most ε , and θ_ℓ has second derivative bounded by M , a local finite difference estimator using samples separated by h satisfies*

$$|\hat{q}_\ell(\rho) - q_\ell(\rho)| \leq 2\varepsilon/h + Mh/2$$

away from the interval endpoints.

Proof. At a fixed ρ , the circle intersects the sector boundaries exactly at the ordered angles

$$\theta_1(\rho), \dots, \theta_L(\rho).$$

Between consecutive boundary angles the label is constant and equal to the corresponding sector type. Therefore the discontinuities of the circular label function are exactly the boundary angles, with their oriented adjacent label pairs. Because the graphs are non-crossing and C^1 , ordering at one radius uniquely associates each discontinuity with the same boundary at all nearby radii; continuation over $[a, b]$ gives the full traces. Differentiability of C^1 traces gives $q_\ell = d\theta_\ell/d\rho$.

For the stability bound, let the measured trace be $\hat{\theta}(\rho) = \theta(\rho) + e(\rho)$ with $|e| \leq \varepsilon$. The one-sided estimator is

$$\hat{q}(\rho) = \frac{\hat{\theta}(\rho + h) - \hat{\theta}(\rho)}{h}.$$

The error from measurement perturbation is at most $(|e(\rho+h)| + |e(\rho)|)/h \leq 2\varepsilon/h$. Taylor's theorem gives truncation error at most $Mh/2$. Adding the two terms proves the stated bound. Centered differences improve constants but are not needed for the identifiability statement. \square

Theorem 3 (Weighted transitive/cyclic decomposition). *Let $G = (V, E)$ be connected, $B \in \mathbb{R}^{|E| \times |V|}$ its oriented incidence matrix, and W a positive diagonal matrix. Every edge-flow vector q has a unique decomposition*

$$q = Bf + c, \quad B^\top Wc = 0, \quad \mathbf{1}^\top f = 0.$$

The cyclic subspace has dimension $|E| - |V| + 1$.

Proof. Consider the strictly convex least-squares problem on the gauge-fixed subspace $\mathbf{1}^\top f = 0$:

$$\min_f (q - Bf)^\top W(q - Bf).$$

Since G is connected, $\text{rank}(B) = |V| - 1$, and B is injective on the gauge-fixed subspace. Hence the minimizer is unique. The normal equations are $B^\top W(q - Bf) = 0$. Setting $c = q - Bf$ gives the decomposition and the orthogonality condition. If two decompositions existed, their difference would be both a gradient and W -orthogonal to every gradient, hence would have zero weighted norm; uniqueness follows. Finally, rank-nullity gives $\dim(\text{im } B) = |V| - 1$, so the W -orthogonal complement inside $\mathbb{R}^{|E|}$ has dimension $|E| - |V| + 1$. \square

Lemma 1 (Cycle certificates for scalar incompatibility). *Let Z be any signed cycle-basis matrix for G : each row records the oriented edge incidences of one fundamental cycle. Then an edge flow q is scalar-compatible if and only if $Zq = 0$. Therefore the cyclic residual in the weighted decomposition is zero if and only if every directed cycle sum vanishes.*

Proof. For any node potential f , the sum of edge differences around a closed cycle telescopes, so $ZBf = 0$. Hence $\text{im}(B) \subseteq \ker(Z)$. A cycle basis has $|E| - |V| + 1$ independent rows, so

$$\dim \ker(Z) = |E| - (|E| - |V| + 1) = |V| - 1.$$

Because G is connected, $\dim \text{im}(B) = |V| - 1$. The inclusion is therefore equality: $\text{im}(B) = \ker(Z)$. Thus $Zq = 0$ exactly when $q = Bf$ for some potential f . In the weighted decomposition, $c = 0$ is equivalent to $q = Bf$, so the same condition is equivalent to zero cyclic residual. \square

Proof of radial clock non-identifiability. The endpoint trace records the accumulated boundary angle $\theta(\rho) = \theta(a) + \int_a^\rho q(u) du$. Let $t = T(\rho)$ be any strictly increasing differentiable physical clock and let $\tilde{t} = h(t)$ for another increasing differentiable bijection h . The rate in the new clock is

$$\tilde{a}(\tilde{t}) = a(h^{-1}(\tilde{t})) \frac{dh^{-1}}{d\tilde{t}}.$$

Changing variables in the integral shows $\int a(t) dt = \int \tilde{a}(\tilde{t}) d\tilde{t}$. Thus the same endpoint trace is produced by infinitely many physical clocks. No endpoint-only algorithm can choose among them. \square

Proof of the minimum complete-contact design theorem. A circular inoculation order is a closed walk on the genotype contact graph: each boundary between adjacent sectors traverses one edge. To observe an unrestricted antisymmetric pairwise game, the walk must cover every edge of K_n . If n is odd, every vertex of K_n has degree $n - 1$, which is even, so K_n is Eulerian. An Euler circuit covers each edge once and has $\binom{n}{2}$ boundaries; no shorter walk can cover all $\binom{n}{2}$ edges.

If n is even, every vertex of K_n has odd degree. Any closed walk has even degree at every vertex in the multigraph of traversed edges. Therefore the walk must duplicate edges so that all n odd vertices become even. One duplicated edge changes parity at two vertices, so at least $n/2$ duplicated edges are necessary. A perfect matching supplies exactly $n/2$ duplicated edges, after which all degrees are even and an Euler circuit exists in the resulting multigraph. The length is therefore $\binom{n}{2} + n/2$, and the lower bound is attained. \square

Theorem 4 (Exact Gaussian cyclicity test). *Suppose $\hat{q} \sim \mathcal{N}(Bf + c, \Sigma)$, where Σ is positive definite and G is connected. Testing $H_0 : c = 0$ with*

$$T = \min_x (\hat{q} - Bx)^\top \Sigma^{-1} (\hat{q} - Bx)$$

gives $T \sim \chi_{|E|-|V|+1}^2$ under H_0 . Under a fixed cyclic alternative c , T is noncentral chi-squared with noncentrality $\delta = c^\top \Sigma^{-1} c$.

Proof. Whiten the observation: $y = \Sigma^{-1/2} \hat{q}$ and $\tilde{B} = \Sigma^{-1/2} B$. Under H_0 , y is a unit-covariance Gaussian with mean in $\text{im}(\tilde{B})$. The statistic T is the squared norm of the orthogonal projection of y onto $\text{im}(\tilde{B})^\perp$. Since G is connected, $\text{rank}(\tilde{B}) = |V| - 1$, so the orthogonal complement has dimension $|E| - |V| + 1$. A squared norm of that many independent standard normal coordinates is chi-squared. With cyclic mean c , the projected mean has squared norm $c^\top \Sigma^{-1} c$, giving the stated noncentral chi-squared law. \square

Corollary 1 (Replicate power scaling). *Suppose R independent replicate edge-flow estimates satisfy $\hat{q}_r \sim \mathcal{N}(Bf + c, \Sigma)$ with common covariance. The pooled cyclicity test has the same null law $\chi_{|E|-|V|+1}^2$ and noncentrality*

$$\delta_R = R c^\top \Sigma^{-1} c.$$

At level α , its power is

$$1 - F_{\chi_k^2(\delta_R)}(\chi_{k,1-\alpha}^2), \quad k = |E| - |V| + 1,$$

where $F_{\chi_k^2(\delta_R)}$ is the noncentral chi-squared CDF.

Proof. The replicate mean has distribution $\bar{q} \sim \mathcal{N}(Bf + c, \Sigma/R)$. Applying the exact Gaussian cyclicity theorem with covariance Σ/R gives the same residual dimension k and noncentrality $c^\top(R\Sigma^{-1})c = Rc^\top\Sigma^{-1}c$. The stated power is the upper tail probability above the central chi-squared level- α threshold. \square

Theorem 5 (Full-path constant drift information). *For aperture increments*

$$\Delta\phi_k \sim \mathcal{N}\left(2w \frac{\Delta r_k}{m_k}, 4D \frac{\Delta r_k}{m_k^2}\right),$$

where $m_k = (r_k + r_{k+1})/2$, the maximum-likelihood estimator of constant wall drift w has Fisher information

$$I(w) = \sum_k \frac{(2\Delta r_k/m_k)^2}{4D\Delta r_k/m_k^2} = \frac{r_N - r_0}{D}.$$

Thus $\text{se}(\hat{w}) = \sqrt{D/(r_N - r_0)}$.

Proof. This is a one-parameter Gaussian linear model with known heteroscedastic variance. The Fisher information is the sum of squared designs divided by variances. Substituting the design and variance cancels m_k and leaves $\Delta r_k/D$. Summing over increments yields $(r_N - r_0)/D$. The least-squares/MLE variance is the reciprocal information. \square

Theorem 6 (Bonferroni-valid interval scan). *For a fixed finite family \mathcal{I} of radial intervals, let p_I be the exact two-sided Gaussian likelihood-ratio p -value for interval I under the zero-drift null. The scan rule that rejects when $\min_{I \in \mathcal{I}} |\mathcal{I}| p_I \leq \alpha$ controls family-wise false positive probability at level α .*

Proof. Each p_I is a valid null p -value, so $\Pr(p_I \leq \alpha/|\mathcal{I}|) \leq \alpha/|\mathcal{I}|$. By the union bound,

$$\Pr\left(\min_I p_I \leq \alpha/|\mathcal{I}|\right) \leq \sum_{I \in \mathcal{I}} \Pr(p_I \leq \alpha/|\mathcal{I}|) \leq \alpha.$$

No independence between overlapping intervals is required. \square

Proposition 3 (Local/global non-identifiability). *If observed edge flow is modeled as $q = Bf + \ell$, where f is a global front-speed potential and ℓ is local pairwise interaction, then endpoint geometry cannot uniquely separate f from ℓ . For any gauge-fixed vector h , $q = B(f + h) + (\ell - Bh)$ gives the same endpoint trace.*

Proof. The endpoint geometry depends only on the sum $Bf + \ell$. Replacing f by $f + h$ and ℓ by $\ell - Bh$ leaves this sum unchanged. Since there are infinitely many admissible h , the separation is not identifiable without additional measurements or constraints. \square